J Mater Sci (2009) 44:3285–3295
DOI 10.1007/s10853-009-3444-5

Effect of different catalyst supports on the (*n,m*) selective growth of single-walled carbon nanotube from Co–Mo catalyst

Bo Wang · Yanhui Yang · Lain-Jong Li · Yuan Chen

Received: 23 January 2009 / Accepted: 27 March 2009 / Published online: 15 April 2009

Abstract Co–Mo catalysts supported on four different high surface area oxides (SiO_2, Al_2O_3, MgO, and TiO_2) were evaluated to investigate the (*n,m*) selectivity control in single-walled carbon nanotube (SWCNT) synthesis. Results from Raman spectroscopy and thermogravimetric analysis showed that Co–Mo catalysts supported on SiO_2 and MgO possessed good selectivity toward SWCNTs, while photoluminescence and ultraviolet–visible–near-infrared spectroscopy results indicated that these two catalyst supports induced the same (*n,m*) selectivity to near-armchair tubes, such as (*6,5*) and (*7,5*) tubes. Catalysts supported on TiO_2 produced a mixture of multi-walled carbon nanotubes (MWCNTs) and SWCNTs, whereas catalysts supported on Al_2O_3 mainly grew MWCNTs. Characterization of catalysts by ultraviolet–visible diffuse reflectance spectroscopy suggested that the surface morphology of metal clusters over different supports was not directly responsible for the (*n,m*) selectivity. Analysis of monometallic (Co or Mo) and bimetallic (Co–Mo) catalysts using temperature program reduction demonstrated that catalyst supports changed the reducibility of metal species. The interaction between supports and Co/Mo metals perturbed the synergistic effect between Co and Mo, leading to the formation of different metal species that are responsible for the observed distinction in SWCNT synthesis.

B. Wang · Y. Yang · Y. Chen (✉)
School of Chemical and Biomedical Engineering, Nanyang Technological University, Singapore 637459, Singapore
e-mail: chenyuan@ntu.edu.sg
URL: www.ntu.edu.sg/home/chenyuan

L.-J. Li
School of Materials Science and Engineering, Nanyang Technological University, Singapore 639798, Singapore

Introduction

The unique electrical and mechanical properties of single-walled carbon nanotubes (SWCNTs) make them ideal candidates for novel molecular devices of various applications [1]. Each (*n,m*) nanotube can be considered as a distinct molecule with unique structure and property because the *n* and *m* indices specify the unique manner in which a single layer of graphite is rolled up seamlessly to form the tube. Common SWCNT synthesis methods produce samples lacking structure and property uniformity. This is one of the primary reasons why SWCNTs are rarely used for commercial applications [2]. Significant efforts have been dedicated to obtain monodisperse SWCNTs through selective synthesis and enrichment [3, 4]. Although (*n,m*) selective growth has not matched or exceeded the degree of control demonstrated by post-synthetic enrichment approaches [3], (*n,m*) narrowly distributed samples show some advantages over samples having a wider diameter distribution in various enrichment processes [5, 6].

Synthesis of SWCNTs in catalytic chemical vapor deposition (CVD) appears promising due to its controllability and potential for high-yield productions [7]. However, CVD SWCNT synthesis is an extremely sensitive catalytic reaction. A narrow SWCNT growth condition window may exist, in which the right balance is necessary between carbon supply and metal cluster nucleation for SWCNT growth [8, 9]. By varying growth conditions, this dynamic balance can be controlled to some extent, leading to the production of SWCNTs with different (*n,m*) distributions. High temperature facilitates the nucleation of metal clusters and solubility of carbon in metal clusters, which changes the nanotube diameter and (*n,m*) distribution [10–13]. The synergistic effect between Co or Fe and Mo or Ru results in

well-dispersed small metal clusters growing SWCNTs with narrow (*n,m*) distribution [10, 14, 15]. Higher carbon monoxide (CO) pressures in a CVD reactor can supply carbon sources faster to metal clusters, allowing production of SWCNTs with smaller diameters [16]. Different carbon precursors can also modify the carbon supply rate in SWCNT growth, which result in tubes with different (*n,m*) distribution [12, 17, 18]. Various crystal planes of sapphire also affect the diameter and (*n,m*) distribution of SWCNTs when tubes are grown aligning on the surface [19, 20].

The SWCNT synthesis catalysts can be prepared by dispersing metal ions on a catalyst support (e.g., a high surface area oxide). Next, metal ions are reduced, which nucleate into small clusters. Metal clusters trigger tube growth under a carbon source. Various catalyst supports, including SiO_2 [14], Al_2O_3 [21], MgO [22], zeolites [23], silica–alumina [24], clay [25], and MCM-41 [26], have been utilized owing to their large surface area, high temperature stability, and simplicity for removal by either acid or alkaline [7]. Lolli et al. [12] have attempted to change the (*n,m*) growth selection by modifying the morphology of metal clusters via their interactions with different catalyst supports. They compared the SWCNT growth from Co–Mo catalysts supported on SiO_2 and MgO, and concluded that smaller chiral angle tubes are produced from MgO-supported catalysts due to the stronger interaction between MgO with Co [12]. Lamouroux et al. [7] further proposed that a strong "metal–support interaction" is necessary to limit the high temperature sintering of metal clusters, but catalyst supports such as TiO_2, which have been reported to have strong interaction with supported metal particles [27], have not been tested in SWCNT growth. Therefore, it is useful to evaluate the feasibility of (*n,m*) selection control through different catalyst supports, which may help to achieve the ultimate goal of (*n,m*) selective growth of SWCNTs.

Driven by this aim, four oxide catalyst supports, including SiO_2, Al_2O_3, MgO, and TiO_2 were studied. Co–Mo bimetallic catalyst was chosen because (1) its optimum composition and metal loading have been systemically studied; [28, 29] and (2) its effectiveness in growing SWCNTs with a narrow (*n,m*) distribution has been demonstrated [14]. In order to systematically elucidate the effect of catalyst supports, SWCNTs were synthesized under the same growth condition while maintaining the Co–Mo molar ratio and loading-to-surface-area ratio constant for all the catalysts. The resulting carbon deposits were evaluated by Raman spectroscopy, thermogravimetric analysis (TGA), photoluminescence (PLE), and ultraviolet–visible–near-infrared radiation (UV–vis–NIR) absorption spectroscopy. Ultraviolet–visible (UV–vis) diffuse reflectance spectroscopy was used to measure the domain size of transition-metal oxides. Reducibility of Co and Mo on different catalyst supports was characterized by H_2-temperature programmed reduction (H_2-TPR).

Experimental methods

Preparation of catalysts

Bimetallic Co–Mo catalysts supported on different catalyst supports (SiO_2, Sigma-Aldrich, No. 288624; Al_2O_3, Sigma-Aldrich, No. 267740; MgO, Sigma-Aldrich, No. 342793; and TiO_2, Degussa, Aeroxide P25) were prepared using the incipient wetness impregnation. The Co (from $Co(NO_3)_2 \cdot 6H_2O$, Sigma-Aldrich, 99.999%) to Mo (from $(NH_4)_6Mo_7O_2 \cdot 4H_2O$, Sigma-Aldrich, 99.98%) molar ratio was fixed at 1:3 molar ratios. Mo loading was 4.6 wt% for SiO_2-supported catalysts with the surface area of 480 m^2/g. The metal contents for other supports, such as Al_2O_3 (155 m^2/g), MgO (145 m^2/g), and TiO_2 (45 m^2/g), were adjusted according to the same loading-to-surface-area ratio. In order to better clarify the role of catalytic supports, monometallic catalysts, Co/support and Mo/support, were also prepared with identical Co or Mo loadings compared to those of Co–Mo/support catalysts. After impregnation, catalysts were dried overnight in an oven at 60 °C and then calcined for 3 h at 500 °C in air. Samples prepared are listed in Table 1.

SWCNT synthesis

A certain amount of calcined catalysts (200 mg of SiO_2-supported catalysts) were loaded in a CVD reactor. The weight of catalysts inside the reactor was varied to maintain a constant metal weight for each synthesis because catalysts were prepared according to the same loading-to-surface-area ratio. Catalysts were firstly prereduced under 1 bar flowing H_2 (50 sccm) using a temperature ramp of 10 °C/min to 500 °C. As soon as the temperature reached 500 °C, the reactor was purged through flowing Ar (500 sccm), while the temperature was continually increased to 800 °C. CO (the carbonyls removed by a Nanochem Purifilter from Matheson Gas Products) was induced (100 sccm) and kept at 6 bar for 1 h. Finally, the reactor was cooled down to room temperature under flowing Ar.

SWCNT characterization

The yield and purity of SWCNTs was monitored by Raman spectroscopy and TGA. Raman spectra of as-synthesized SWCNTs were collected on a Renishaw Raman spectroscopy equipped with both 514- and 633-nm lasers. TGA was

Table 1 Synthesized Co, Mo, and Co–Mo catalysts supported on various catalyst supports

	Support	Metal content (wt%)		Surface area (m^2/g)	Metal/surface area (μmol/m^2)	
		Co	Mo		Co	Mo
Co/SiO_2	SiO_2	0.942	–	480	0.333	–
Mo/SiO_2	SiO_2	–	4.6		–	0.999
$Co–Mo/SiO_2$	SiO_2	0.942	4.6		0.333	0.999
Co/Al_2O_3	Al_2O_3	0.304	–	155	0.333	–
Mo/Al_2O_3	Al_2O_3	–	1.486		–	0.999
$Co–Mo/Al_2O_3$	Al_2O_3	0.304	1.486		0.333	0.999
Co/MgO	MgO	0.285	–	145	0.333	–
Mo/MgO	MgO	–	1.39		–	0.999
Co–Mo/MgO	MgO	0.285	1.39		0.333	0.999
Co/TiO_2	TiO_2	0.0883	–	45	0.333	–
Mo/TiO_2	TiO_2	–	0.431		–	0.999
$Co–Mo/TiO_2$	TiO_2	0.0883	0.431		0.333	0.999

conducted on a PerkinElmer Diamond TG/DTA equipment. For carbon deposits grown from $Co–Mo/SiO_2$, SiO_2 was removed by refluxing in 1.5 mol/L NaOH solution for 2 h before TGA. For carbon deposits grown from Co–Mo/MgO, MgO was removed by washing with 2 mol/L HCl solution. On the other hand, for carbon deposits grown from $Co–Mo/Al_2O_3$ and $Co–Mo/TiO_2$, as-synthesized catalysts loaded with carbon were used in TGA since there is no simple way to remove these two catalyst supports from carbon deposits.

The (n,m) distribution of SWCNTs was characterized by PLE and UV–vis–NIR absorption spectroscopy. The PLE was conducted on a Jobin-Yvon Nanolog-3 spectrofluorometer with the excitation scanned from 300 to 850 nm and the emission collected from 900 to 1,400 nm. The UV–vis–NIR absorption spectra were measured on Varian Cary 5000 UV–vis–NIR spectrophotometer. The SWCNT suspensions were obtained by recovering tubes from catalyst supports and dispersing them in surfactant solutions. Carbon deposits (2 mg) were suspended in 5 mL of 2 wt% sodium cholate (SC) (Sigma Ultra)/D_2O solution by sonication using a cup-horn sonicator (SONICS, VCX-130) at 20 W for 1 h. After sonication, the suspensions were centrifuged for 1 h at 80,000g to precipitate residual particles and large aggregates of nanotubes. The stable semitransparent dispersions were extracted for the subsequent spectroscopy analysis.

Catalyst characterization

The Brunauer–Emmett–Teller (BET) surface areas of different supports were determined through N_2 adsorption/desorption isotherms obtained with a static volumetric instrument Autosorb-1C (Quanta Chrome). The morphology of the metal clusters was investigated by UV–vis diffuse reflectance spectroscopy using a Varian Cary 5000 UV–vis–NIR spectrophotometer with a praying-mantis diffuse reflectance accessory. Adopting the procedure described in a previous study, the square root of Kubelka-Munk function multiplied by the photon energy was plotted as a function of photon energy [30]. The reflectance of $BaSO_4$ was used as a reference. The reducibility of calcined catalysts was characterized by H_2-TPR using the thermal conductivity detector (TCD) of a gas chromatography (Techcomp, 7900). Approximately 200 mg of each sample was loaded into a quartz cell. Prior to each TPR run, the sample cell was purged with air at room temperature. The cell temperature was increased to 500 °C at 5 °C/min, soaked for 1 h at 500 °C, and cooled to room temperature. This procedure produces a clean surface before running the H_2-TPR. The gas flow was switched to 5 vol% H_2 in Ar, and the baseline was monitored until it becomes stable. After baseline stabilization, the sample cell was heated at 5 °C/min and held for 30 min at 900 °C. An acetone trap was installed between the sample cell and the TCD to condense water produced during sample reduction.

Results and discussion

Raman spectroscopy of carbon deposits

Raman spectroscopy is commonly used for SWCNT assessment. Figure 1 shows Raman spectra of carbon deposits grown from Co–Mo catalysts supported on SiO_2, Al_2O_3, MgO, and TiO_2. The radial breathing mode (RBM) is the fingerprint for SWCNT structure identification [31]. Strong RBM peaks (between 100 and 400 cm^{-1}) are displayed in Fig. 1 for carbon deposits grown from Co–Mo catalysts supported on SiO_2 and MgO. Under a 514-nm

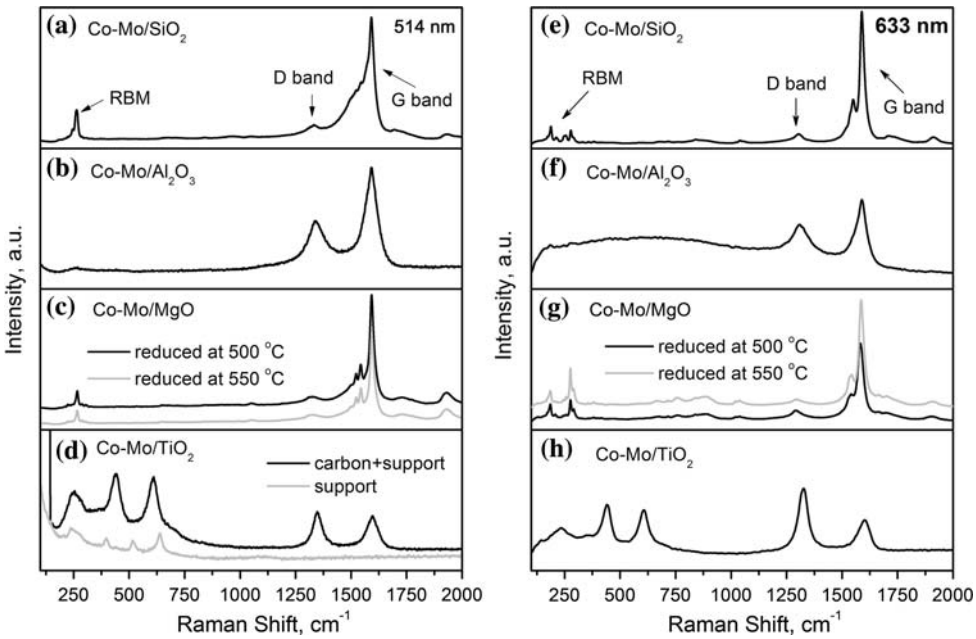

Fig. 1 Raman spectra of carbon deposits grown from Co–Mo catalysts supported on SiO_2, Al_2O_3, MgO, and TiO_2: **a–d** are under 514-nm laser excitation; **e–h** are under 633-nm laser excitation

laser excitation (Fig. 1a, c), the dominant RBM peaks for Co–Mo/SiO_2 and Co–Mo/MgO are both centered at around 266 cm^{-1}. It suggests that SWCNTs grown from Co–Mo/MgO are similar in diameter compared to tubes grown from Co–Mo/SiO_2 because the RBM peak position is inversely proportional to the diameter of SWCNT [31]. Raman spectra conducted under a 633-nm laser excitation (Fig. 1e, g) also reveal that Co–Mo/SiO_2 and Co–Mo/MgO grow the same tube species. The RBM peaks of tubes from Co–Mo/MgO are more intense at the higher wavenumber region (278 cm^{-1}). Due to the resonance effect, it is difficult to accurately determine the (*n,m*) distribution of a SWCNT sample using Raman spectroscopy. The (*n,m*) distribution of SWCNTs produced on Co–Mo/SiO_2 and Co–Mo/MgO were characterized by PLE and UV–vis–NIR spectroscopy, which will be discussed later.

Figure 1b and f show that carbon deposits from Co–Mo/Al_2O_3 have no RBM peaks, suggesting that Co–Mo/Al_2O_3 is not selective for SWCNT growth. Furthermore, the single-peak featured G bands (1,590 cm^{-1}) and the intense D bands (1,310 cm^{-1}) on Fig. 1b and f demonstrate the presence of multi-walled carbon nanotubes (MWCNTs) or graphite [32]. For carbon deposits grown on Co–Mo/TiO_2, Raman spectra of carbon deposits, shown in Fig. 1d and h, are strongly affected by Raman features of TiO_2 support. TiO_2 was characterized to elucidate its impact on Raman spectra. Degussa P25 used is a mixture of 80% anatase and 20% rutile. The Raman spectrum (gray curve in Fig. 1d) from fresh TiO_2 displays several peaks, similar to previous studies [33]. However, after impregnating metal ions, calcination, and SWCNT growth, Raman spectrum in the RBM region of Co–Mo/TiO_2 resembles that of pure rutile TiO_2 [33]. The structural change of TiO_2 is beyond the scope of this study. An important message is that the RBM peaks on Fig. 1d are mainly contributed by TiO_2 rather than SWCNTs. Based on the shape of G band and D band on Fig. 1d and h, we conclude that Co–Mo/TiO_2 is more selective for MWCNT growth than SWCNT growth.

TGA of carbon deposits

In order to further verify the results obtained by Raman spectroscopy, TGA was applied to distinguish carbon species in the carbon deposits produced. TGA profiles of carbon nanotube samples can be categorized into three oxidation regions: amorphous carbon below 300 °C, carbon nanotubes (SWCNTs and MWCNTs) between 400 and 700 °C, and graphite above 800 °C [34]. When metal residues are present, positive peaks may appear in the differential thermogravimetric (DTG) profiles due to the weight increase of samples from the oxidation of metal residues. Moreover, metal residues can catalyze the oxidation of carbon species, and oxidation temperatures of carbon species may shift significantly [8, 35]. This complicates the assignment of SWCNT and MWCNT peaks in a TGA profile. Figure 2 shows the TGA profiles of carbon deposits grown from four different supports. In Fig. 2a, weak peaks from amorphous carbon (below 300 °C) can be observed. Both the two major DTG peaks centered at 420 and 530 °C can be assigned to SWCNTs, as in the case of a previous study [8]. The two oxidation peaks from SWCNTs are caused by different interactions between SWCNTs and metal residues. The weak and broad peaks around 800 °C come from Mo residues. Figure 2b

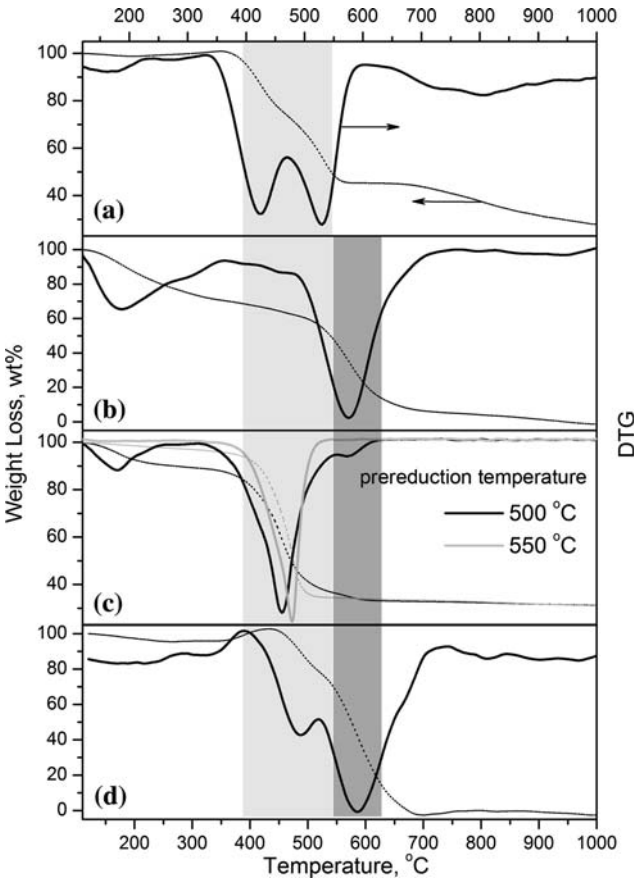

Fig. 2 TGA of carbon deposits from: **a** Co–Mo/SiO_2; **b** Co–Mo/Al_2O_3; **c** Co–Mo/MgO; **d** Co–Mo/TiO_2. Weight loss profiles are dotted lines, while the corresponding DTG profiles are solid lines. The proposed temperature regions for oxidation of SWCNTs and MWCNTs are highlighted in light gray and dark gray, respectively

demonstrates that carbon deposits grown on Co–Mo/Al_2O_3 are mainly amorphous carbon and MWCNTs; this is consistent with Raman results presented in Fig. 1. Figure 2c illustrates that most carbon deposits grown on Co–Mo/MgO are SWCNTs, having one oxidation peak at 460 °C. The DTG results in Fig. 2d demonstrate the presence of MWCNTs in carbon deposits grown from Co–Mo/TiO_2, which is consistent with Raman results shown in Fig. 1. Moreover, DTG in Fig. 2d also indicates the presence of SWCNTs.

(*n,m*) distribution of SWCNTs

Since only Co–Mo/SiO_2 and Co–Mo/MgO are selective to SWCNTs, as indicated by Raman spectroscopy and TGA, further evaluation toward their (*n,m*) and diameter distributions were conducted on these two samples. The resonance behavior of both excitation and emission events results in spikes corresponding to transition pairs from individual (*n,m*) SWCNTs. The PLE maps in Fig. 3 show that SWCNTs with narrow (*n,m*) distribution were produced using both Co–Mo/SiO_2 and Co–Mo/MgO. In order to confirm that the observed narrow (*n,m*) distribution is not induced by our dispersion or centrifugation, SWCNTs were also dispersed by two other surfactants separately: sodium dodecyl benzene sulfonate (SDBS) and sodium dodecyl sulfate (SDS). Furthermore, the dispersed SWCNT solutions were centrifuged under different centrifugation forces ranging from 20,000 to 120,000*g* prior to PLE studies. In subsequent PLE studies, no significant changes in their (*n,m*) distribution were observed as compared to those results shown in Fig. 3. In order to estimate the abundance of various (*n,m*) tubes, we assume that PLE intensities are proportional to tube abundances. PLE efficiencies of various (*n,m*) species were not considered here because a recent experimental study on individual tubes recommends that the actual PLE efficiency differences among various (*n,m*) species may not be as large as the theoretical estimations of a previous study [36]. In order to minimize the influence of varying spectrum backgrounds, PLE intensities were determined from the amplitude of the partial derivatives of each single emission profile extracted from PLE maps [37]. Figure 3d–f present the (*n,m*) abundance for each species identified in PLE maps as a function of its diameter. The abundance and the properties of identified (*n,m*) species are also listed in Table 2. Based on PLE maps, (*7,5*) *is* the most dominating species, and SWCNTs from both Co–Mo/SiO_2 and Co–Mo/MgO have a narrow diameter distribution.

The dispersed SWCNT solutions were also characterized by UV–vis–NIR absorption spectroscopy. The UV–vis–NIR spectra shown in Fig. 4 reaffirmed that SWCNTs from Co–Mo/MgO contain more tube species with smaller diameter than those from Co–Mo/SiO_2. More specifically, SWCNTs from Co–Mo/MgO contains more (*8,3*) and (*6,5*) tubes, as highlighted in light gray color. The highlighted light gray color peaks (from (*8,3*) and (*6,5*) tubes) of spectra b and c in Fig. 4 are more intense relative to the gray color peaks from (*7,5*) tubes. This is different from the PLE results in Fig. 3, in which peaks from (*7,5*) tubes have the highest intensity. The similar differences between UV–vis–NIR and PLE have been observed in our previous study [16]. There are two reasons which may explain the apparent discrepancy between UV–vis–NIR and PLE results: (1) The absorption peaks of (*6,5*) and (*8,3*) tubes are overlapped. Both (*8,3*) and (*6,5*) may contribute to the same broad absorption peak in UV–vis–NIR spectra, while they are clearly separated in PLE maps. (2) Different (*n,m*) species have different absorption and PLE efficiency, which may lead to dissimilar peak intensities in UV–vis–NIR and PLE spectroscopy. Further detailed study is required to elucidate the intensity variation among various (*n,m*) tubes in UV–vis–NIR and PLE spectroscopy.

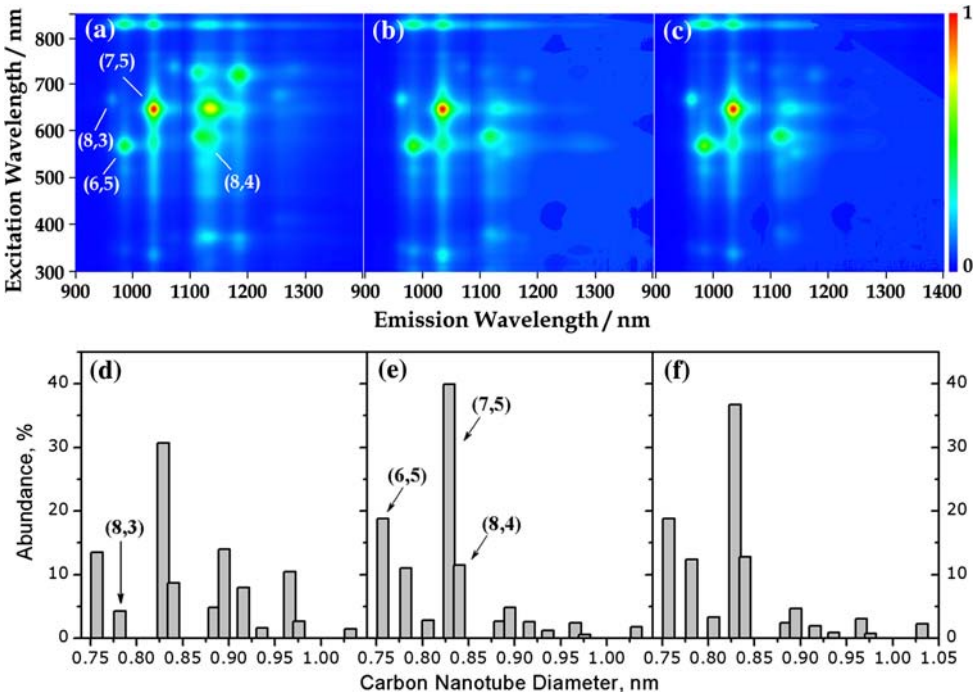

Fig. 3 Two-dimensional excitation versus emission PLE contour maps of SWCNTs from: **a** Co–Mo/SiO_2, prereduced at 500 °C; **b** Co–Mo/MgO, prereduced at 500 °C; and **c** Co–Mo/MgO, prereduced at 550 °C. Calculated diameter distribution histograms of SWCNTs obtained from corresponding PLE contour maps: **d** from **a**; **e** from **b**; and **f** from **c**

Table 2 Abundance of (*n,m*) tubes from Co–Mo/SiO_2 and Co–Mo/MgO determined by PLE

(*n,m*)	Diameter (nm)	Chiral angle (degree)	E_{11}^{a} (nm)	E_{22}^{b} (nm)	SiO_2, 500 °C	MgO, 500 °C	MgO, 550 °C
(6,5)	0.757	27.0	986	570	13.46	18.76	18.79
(8,3)	0.782	15.3	962	666	4.30	10.98	12.35
(9,2)	0.806	9.8	1,144	552	0.00	2.79	3.34
(7,5)	0.829	24.5	1,036	646	30.68	39.92	36.75
(8,4)	0.840	19.1	1,120	590	8.66	11.46	12.81
(10,2)	0.884	8.9	1,070	736	4.83	2.69	2.44
(7,6)	0.895	27.5	1,134	648	13.96	4.81	4.69
(9,4)	0.916	17.5	1,112	726	7.94	2.60	1.90
(10,3)	0.936	12.7	1,258	648	1.58	1.20	0.91
(8,6)	0.966	25.3	1,182	722	10.49	2.40	3.06
(9,5)	0.976	20.6	1,254	680	2.65	0.60	0.72
(8,7)	1.032	27.8	1,274	732	1.46	1.79	2.24

[a, b] Excitation and absorption energies, respectively, of (*n,m*) tubes were determined by spike positions observed on PLE maps shown in Fig. 3

As claimed by Lolli et al. [12], MgO-supported catalysts are more selective to small chiral angle tubes (e.g., (*8,4*)) compared to SiO_2-supported catalysts. Their claim was obtained by evaluating (*n,m*) abundance through fitting absorption spectra of different samples [12]. However, we find that their absorption spectrum-fitting method may have underestimated the abundance of smaller chiral angle tubes (e.g., (*8,3*)) produced from SiO_2-supported catalysts. As illustrated in Fig. 5, (*8,3*) has a similar diameter as (*6,5*), while (*8,4*) has a similar diameter as (*7,5*). E_{11} transition energies of (*7,5*) and (*8,4*) are quite different at 1,028 and 1,116 nm, respectively, as listed in Table 2. It is relatively simple to differentiate the contribution from those two species on absorption spectra. However, E_{11} transition energies of (*6,5*) and (*8,3*) are closer at 989 and 955 nm, respectively, which makes them harder to be deconvolved from absorption spectra, as illustrated in Fig. 4. In contrast, PLE results in Fig. 3 clearly highlight the existence of (*8,3*) tubes from SiO_2-supported catalysts. As shown in Fig. 5, (*8,3*) has even smaller chiral angle than (*8,4*) (15.3 vs. 19.1°). Therefore, we conclude that the MgO-supported catalysts do not possess particular selectivity toward smaller chiral angle tubes compared to SiO_2-supported catalysts.

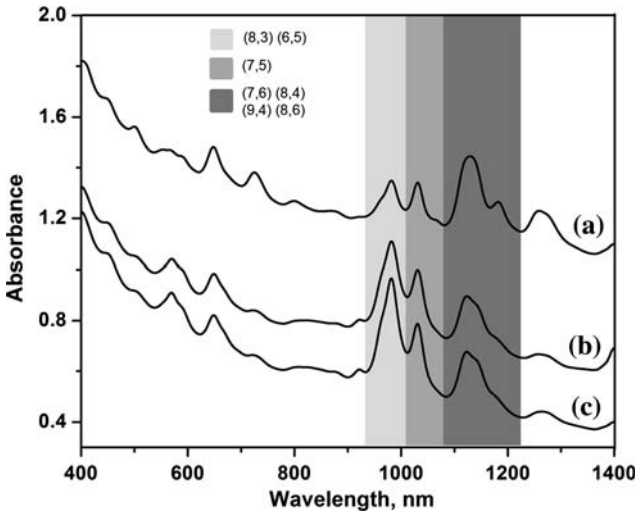

Fig. 4 UV–vis–NIR spectra of SC-dispersed SWCNTs from: **a** Co–Mo/SiO_2; **b** Co–Mo/MgO reduced at 500 °C; and **c** Co–Mo/MgO reduced at 550 °C. The relative absorption peaks at E_{11} transitions for tubes with different diameters are highlighted

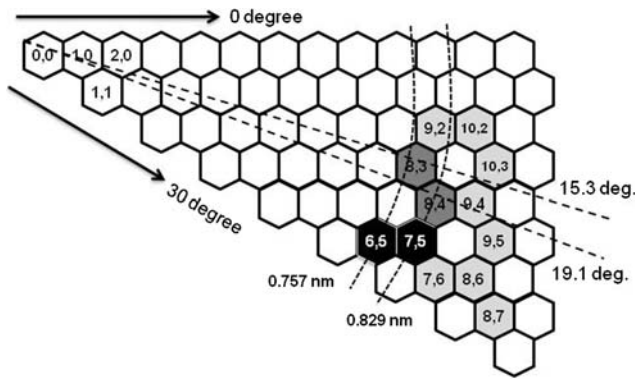

Fig. 5 (*n,m*) maps of SWCNTs from Co–Mo/SiO_2 and Co–Mo/MgO. Tubes detected in PLE were highlighted in gray and black colors

The role of supports in (*n,m*) selective SWCNT growth

There are two unexpected findings in our SWCNT characterization results: (1) MgO- and SiO_2-supported catalysts produce SWCNTs with similar (*n,m*) distribution, although MgO is known to interact more strongly with Co than SiO_2, and to form solid solutions with Co ions [12]. (2) TiO_2-supported catalysts are not (*n,m*) selective, although reducible TiO_2 exhibits strong interaction with group VIII metals [27]. The influence of the catalyst supports on the stabilization of metal particles usually can be explained by several dynamic processes such as: encapsulation or mechanical trapping, formation of new chemical compounds, alloying with the elements constituting the lattice of support, and anchoring of the metal particle by the surface sites [38].

Lolli et al. [12] reported that domain size of small metal oxides can be changed because of the different interactions between supports and metals leading to the growth of SWCNTs at different chiral angles. However, our results in PLE and UV–vis–NIR studies present a different trend. In order to clarify the influence of metal oxide domain size changes, we applied the UV–vis diffusive reflectance spectroscopy to measure the band energy gap of catalysts, which is inversely proportional to the metal-oxide domain size. As recommended [12, 30], we used the square root of the Kubelka-Munk function multiplied by the photon energy, and plotted the resulting function versus the photon energy. The spectral data for calcined Co–Mo catalysts supported on four different catalyst supports are shown in Fig. 6. Energy gaps of two references (indicated in Fig. 6) were also calculated to validate our experimental procedure. SiO_2-supported catalysts have a band gap of 3.25 eV, while MgO-supported catalysts have a band gap of 3.4 eV, indicating that MgO-supported catalysts have a smaller metal-oxide domain size than SiO_2-supported catalysts. However, disordered metal clusters on MgO do not produce SWCNTs significantly different from those found on SiO_2. Apart from this, Al_2O_3-supported catalyst has a smaller metal oxide domain size (band gap of 3.6 eV) than than TiO_2-supported catalyst (band gap of 2.94 eV); however, both TiO_2- and Al_2O_3-supported catalysts are not selective to SWCNT growth. These results consistently demonstrate that different domain sizes of metal oxides induced by various catalyst supports are not directly responsible for the (*n,m*) selective growth of SWCNTs.

The chemistry of the metal–support interaction is one of the key factors to understand the catalytic performance of

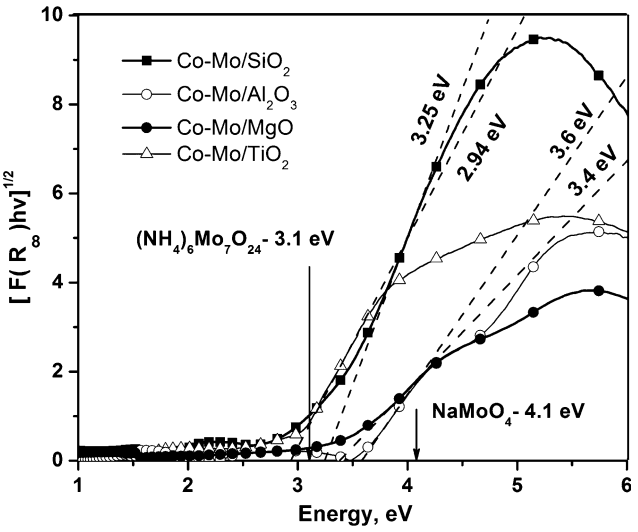

Fig. 6 Diffusive reflectance band-gap extrapolation for Co–Mo catalysts supported on four different catalyst supports. Gaps for two reference compounds are pointed using arrows

different catalysts [38]. TPR is a useful characterization technique for investigating the chemistry of the metal-support interaction and surface chemical information (e.g., material species, stability, and metal distribution) [39]. Figure 7 shows the TPR profiles of metal species on four catalyst supports. For each support, monometallic Co and Mo catalysts were compared to bimetallic Co–Mo catalysts in order to reveal the possible synergistic effect between Co and Mo.

Figure 7a presents TPR profiles of catalysts supported on SiO_2. The first two peaks on the TPR profile of Co supported on SiO_2 are at 380 and 470 °C, respectively, which are due to the Co reduction under H_2 according to these steps: $Co_3O_4 \rightarrow CoO \rightarrow Co$ [40]. Co oxides (Co_3O_4 and CoO) were formed during the calcination of catalysts. They can be reduced at relatively low temperatures and are likely to form large metal particles under high-temperature reduction during SWCNT growth. The peak above 900 °C can be attributable to the reduction of Co silicates (Co_2SiO_4 and Co_2SiO_4) [41]. Co silicates are formed through the strong interaction between Co ions and SiO_2 support. Because of their less reducibility, it is difficult to reduce Co silicates for SWCNT growth. The TPR profile of monometallic Mo supported on SiO_2 has one major peak at 770 °C, which can be explained by the reduction of MoO_3 (formed in calcination) in two steps: $MoO_3 \rightarrow MoO_2 \rightarrow Mo$ [42, 43]. With the assistance of TPR profiles from monometallic Co and Mo catalysts, the peaks on the TPR profile of Co–Mo catalyst supported on SiO_2 can be allocated accordingly. It should be noted that the peak of Co silicates is absent on the TPR profile of Co–Mo catalyst. This may be due to the presence of Mo, which may curb the interaction between Co ions and SiO_2 to form Co silicates. Nonetheless, the most important feature related to SWCNT growth is the new peak at 575 °C, as highlighted in gray color. This peak can be attributed to the reduction of $CoMoO_4$ adopting a route of $CoMoO_4 \rightarrow CoMoO_3 \rightarrow Co_3Mo \rightarrow Co_2Mo_3$, in which Co ions are well dispersed by Mo [41, 42]. The existence of $CoMoO_4$ has previously been verified by X-ray diffraction [41, 42]. The highly dispersed Co ions are then further reduced by CO forming small metal clusters that result in (n,m) selective SWCNT synthesis.

Figure 7b shows TPR profiles of catalysts supported on Al_2O_3. It can be noted that the reduction peak at 570 °C for monometallic Mo supported on Al_2O_3 is very small, as compared with that in TPR profiles of catalysts supported on SiO_2. However, a large peak can be observed above 900 °C. Previous TPR and XRD studies on Mo catalysts indicated that Al_2O_3 interact strongly with Mo oxides to form tetrahedral Mo species that are difficult to be reduced [44]. This accounts for the Mo reduction peak above 900 °C. The TPR profile of Co–Mo catalyst supported on Al_2O_3 also presents a large peak above 900 °C, suggesting that most Mo species still interact strongly with Al_2O_3

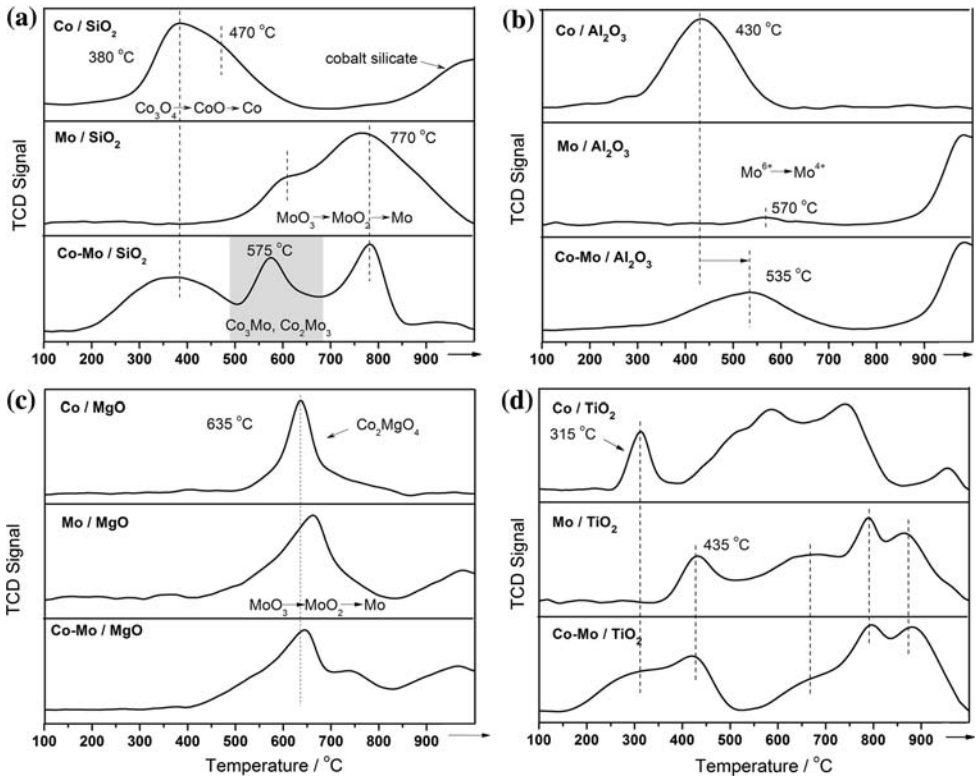

Fig. 7 TPR profiles of monometallic Co, Mo and bimetallic Co–Mo catalysts supported on various catalyst supports: **a** SiO_2, **b** Al_2O_3, **c** MgO, and **d** TiO_2

rather than Co. TPR peaks of Co oxides upshift to 535 °C, which is still significantly lower than the 575 °C peak of SiO_2-supported catalyst. Therefore, we propose that there is a strong interaction between Mo and Al_2O_3, interrupting the synergistic effect between Co and Mo. In the absence of interaction with Mo, Co species are easily reduced to form larger metal particles that are more selective for MWCNTs than for SWCNTs.

Figure 7d also illustrates the interruption of the synergistic effect between Co and Mo supported on TiO_2. TiO_2 possess strong interaction with metal species, which is confirmed by the multiple peaks of monometallic Co and Mo catalysts. No intense peaks exist between 500 and 600 °C on the TPR profile of Co–Mo catalyst. We propose that the absence of these peaks is caused by the strong interactions of Co or Mo with TiO_2 individually, which disrupts the synergistic effect between Co and Mo. Moreover, part of Co oxides supported on TiO_2 can be easily reduced, as indicated by the peak at 315 °C. Even though some Co species (which are reduced at higher temperature) can bring about the growth of SWCNTs, Co–Mo/TiO_2 interactions produce large amount of MWCNTs owing to Co species being reduced at low reduction temperatures.

Figure 6c illustrates different TPR profiles for catalysts supported on MgO. A strong peak contributed by $MgCo_2O_4$ species is observed at 635 °C for monometallic Co catalyst [45]. The TPR profile of monometallic Mo catalyst also shows one major peak that belongs to the reduction of MoO_3. The main peak of Co–Mo catalyst suggests a strong interaction between Co and Mo. The reduction temperature of $CoMoO_4$ is upshifted by 70 °C compared to the SiO_2-supported Co–Mo catalyst (Fig. 7a). This upshifted temperature may be the reason for a greater number of smaller diameter SWCNTs being produced on MgO-supported catalyst, as indicated in Fig. 3. Since the reduction temperature of the monometallic Co catalyst on MgO is almost the same as the Co–Mo catalyst, an intriguing question may arise: whether or not Co/MgO and Co–Mo/MgO have the same performance in SWCNT synthesis? In order to find an answer this question, we tested Co/MgO in SWCNT growth. After 500 °C prereduction in H_2 and growth under CO at 800 °C, small amount of carbon deposits were observed. The MWCNTs were the main species inside this carbon deposits, suggesting that the $MgCo_2O_4$ species formed on Co/MgO are different from Co ions dispersed by Mo from Co–Mo/MgO. This finding also confirms that the synergistic effect between Co and Mo is critical for good SWCNT selectivity.

In our SWCNT synthesis experiments, all the catalysts have been prereduced in H_2 at 500 °C for better comparison among different samples. Based on the TPR profile of MgO-supported catalysts in Fig. 7c, 500 °C may not be the optimum reduction temperature for Co–Mo/MgO. Therefore, another batch of SWCNTs was synthesized at 550 °C prereduction temperature in H_2 using Co–Mo/MgO, considering that the reduction peak of $CoMoO_4$ is upshifted by 70 °C. Raman spectra of the SWCNT samples were shown in Fig. 1. Compared with spectra from SWCNT samples reduced at 500 °C, a stronger RBM can be found. This suggests that more SWCNTs were produced, because more metal Co clusters are available after prereduction at a higher temperature. TGA profile in Fig. 2 also indicates that less amorphous carbon was produced, hence it is more selective to SWCNTs. Furthermore, no considerable changes were observed in the (n,m) selectivity in Figs. 3 and 4, indicating that the prereduction temperature change on Co–Mo/MgO has no significant impact on its (n,m) selectivity.

Based on TPR results and the structure of carbon produced on different catalyst supports, we propose that the formation of $CoMoO_4$, in which Co ions are well dispersed by Mo, is critical for a good SWCNT selectivity on catalysts impregnated with Co. Previous studies have shown that the selectivity of the Co–Mo catalyst strongly depends on the stabilization of Co by Mo oxide. The non-interacting Co phase is reduced to metallic Co that is not selective to SWCNTs, while the Co phase interacting with Mo remains as well-dispersed Co ions that are highly selective to SWCNT production [46]. In this study, we further demonstrate that cobalt oxides, cobalt silicates, and solid solutions such as $MgCo_2O_4$ are all not selective to SWCNT growth. TPR results indicate that different catalyst supports may perturb the interaction between Co and Mo species, leading to the formation of different Co phases responsible for the observed differences in carbon growth. That is, SiO_2 and MgO supports enhance the selectivity toward SWCNTs in a narrow diameter range between 0.75 and 0.85 nm, because the formation of well-dispersed $CoMoO_4$. In contrast, Al_2O_3 and TiO_2 have strong interactions with Co or Mo individually, which disrupts the synergistic effect between Co and Mo. Co–Mo catalysts supported on these two supports are not selective to SWCNTs.

Two conditions must be satisfied for the selective growth of particular (n,m) tubes. First, metallic clusters with narrow diameter distribution should be stabilized during growth, which would manage the diameter variation of SWCNTs. Second, the chiral angle of SWCNTs at a particular diameter should be controlled. This study shows that SiO_2 and MgO provide well-dispersed Co species on Mo oxides, which result in Co clusters in a narrow diameter range suitable for SWCNT growth with diameter between 0.75 and 0.85 nm under CO at 800 °C. However, we cannot elucidate how the chiral angle is manipulated based on current results. Several theoretical studies have proposed that the nanotube chirality is controlled by the formation of carbon cap structure on a metal nanoparticle

catalyst [47, 48]. An interesting observation from this study and previous publications [10, 14, 15, 17] is that most of the narrow (*n,m*) selective SWCNT synthesis produces tubes in the same near-armchair range including (*6,5*), (*7,5*), and (*7,6*) tubes. A recent study has shown that near-zigzag tubes can be grown on the A-plane of sapphire [19]. In contrast to the aligned growth on sapphire planes, oxide supports examined in this study would have limited contact with growing SWCNTs. Oxide catalyst supports are unlikely to change the chiral angle of tubes after the carbon cap structures are formed on metal clusters. Thus, the role of catalyst supports could be limited to regulate the formation of metal clusters. More research is needed to understand the chiral angle selectivity in SWCNT growth.

Finally, in terms of large scale SWCNT production, an essential criterion for choosing a catalyst support lies in its simplicity of removal after SWCNT growth. In this aspect, SiO_2 and MgO are superior to TiO_2 and Al_2O_3. SiO_2 can be removed by alkaline solution, while MgO can be removed in dilute acid solution. Moreover, SiO_2 nanoparticles have larger surface areas than MgO, which implies that more metal ions can be loaded to produce more SWCNTs using the same amount of catlayts.

Conclusions

Co–Mo catalysts supported on four catalyst supports (SiO_2, Al_2O_3, MgO, and TiO_2) were evaluated for SWCNT growth. SiO_2- and MgO-supported catalysts have good selectivity toward SWCNTs; however, there are no significant differences in their (*n,m*) selectivities. Both supports initiate the growth of near-armchair tubes; even though MgO-supported catalysts produce more tubes with slightly smaller diameter due to their less reducibility. TiO_2-supported catalysts produce a mixture of MWCNTs and SWCNTs, while Al_2O_3-supported catalysts mainly produce MWCNTs. UV–vis diffuse reflectance spectroscopy study of catalysts demonstrates that the domain size of metal oxides on various supports is not directly responsible for the (*n,m*) selectivity. TPR analyses of monometallic catalysts (Co and Mo) and bimetallic catalysts (Co–Mo) indicate that supports can change the reducibility of metal species. The different supports may perturb the interaction between Co and Mo species, leading to the formation of diverse metal clusters responsible for the distinction observed in SWCNT synthesis.

Acknowledgements This study was supported by Nanyang Technological University (AcRF Grants RG38/06 and RG106/06), Defense Science & Technology Agency, Singapore (MINDEF-NTU-JPP/08/03) and National Research Foundation, Singapore (NRF-CRP2-2007-02).

References

1. Jorio A, Dresselhaus G, Dresselhaus MS (2008) In: Carbon nanotubes, advanced topics in the synthesis, structure, properties and applications. Springer, Berlin, p 1
2. Joselevich E, Dai H, Liu J, Hata K, Windle AH (2008) Top Appl Phys 111:101
3. Hersam MC (2008) Nat Nanotechnol 3:387
4. Peng X, Komatsu N, Bhattacharya S, Shimawaki T, Aonuma S, Kimura T, Osuka A (2007) Nat Nanotechnol 2:361
5. Chen F, Wang B, Chen Y, Li L-J (2007) Nano Lett 7:3013
6. Wei L, Wang B, Goh TH, Li L-J, Yang Y, Chan-Park MB, Chen Y (2008) J Phys Chem B 112:2771
7. Lamouroux E, Serp P, Kalck P (2007) Cat Rev - Sci Eng 49:341
8. Chen Y, Ciuparu D, Lim S, Haller GL, Pfefferle LD (2006) Carbon 44:67
9. Chen Y, Wang B, Li L-J, Yang Y, Ciuparu D, Lim S, Haller GL, Pfefferle LD (2007) Carbon 45:2217
10. Miyauchi YH, Chiashi SH, Murakami Y, Hayashida Y, Maruyama S (2004) Chem Phys Lett 387:198
11. Ago H, Imamura S, Okazaki T, Saitoj T, Yumura M, Tsuji M (2005) J Phys Chem B 109:10035
12. Lolli G, Zhang LA, Balzano L, Sakulchaicharoen N, Tan YQ, Resasco DE (2006) J Phys Chem B 110:2108
13. Yao Y, Li Q, Zhang J, Liu R, Jiao L, Zhu YT, Liu Z (2007) Nat Mater 6:283
14. Bachilo SM, Balzano L, Herrera JE, Pompeo F, Resasco DE, Weisman RB (2003) J Am Chem Soc 125:11186
15. Li X, Tu X, Zaric S, Welsher K, Seo WS, Zhao W, Dai H (2007) J Am Chem Soc 129:15770
16. Wang B, Wei L, Yao L, Li LJ, Yang YH, Chen Y (2007) J Phys Chem C 111:14612
17. Wang B, Poa CHP, Wei L, Li LJ, Yang YH, Chen Y (2007) J Am Chem Soc 129:9014
18. Malgas GF, Arendse CJ, Cele NP, Cummings FR (2008) J Mater Sci 43:1020. doi:10.1007/s10853-007-2230-5
19. Ishigami N, Ago H, Imamoto K, Tsuji M, Iakoubovskii K, Minami N (2008) J Am Chem Soc 130:9918
20. Wen CY, Huang CC, Cheng HZ, Lu HY (2008) J Mater Sci 43:123. doi:10.1007/s10853-007-2122-8
21. Colomer JF, Bister G, Willems I, Konya Z, Fonseca A, Van Tendeloo G, Nagy JB (1999) Chem Commun 1343
22. Colomer JF, Stephan C, Lefrant S, Van Tendeloo G, Willems I, Konya Z, Fonseca A, Laurent C, Nagy JB (2000) Chem Phys Lett 317:83
23. Hiraoka T, Kawakubo T, Kimura J, Taniguchi R, Okamoto A, Okazaki T, Sugai T, Ozeki Y, Yoshikawa M, Shinohara H (2003) Chem Phys Lett 382:679
24. Cassell AM, Raymakers JA, Kong J, Dai HJ (1999) J Phys Chem B 103:6484
25. Destree A, Long GJ, Vatovez B, Grandjean F, Fonseca A, Nagy JB, Fransolet AM (2007) J Mater Sci 42:8671. doi:10.1007/s10853-007-1808-2
26. Lim S, Ciuparu D, Pak C, Dobek F, Chen Y, Harding D, Pfefferle L, Haller G (2003) J Phys Chem B 107:11048
27. Haller GL, Resasco DE (1989) Adv Catal 36:173
28. Herrera JE, Balzano L, Borgna A, Alvarez WE, Resasco DE (2001) J Catal 204:129
29. Shajahan M, Mo YH, Fazle Kibria AKM, Kim MJ, Nahm KS (2004) Carbon 42:2245
30. Barton DG, Shtein M, Wilson RD, Soled SL, Iglesia E (1999) J Phys Chem B 103:630
31. Dresselhaus MS, Dresselhaus G, Jorio A (2007) J Phys Chem C 111:17887

32. Jorio A, Saito R, Dresselhaus G, Dresselhaus MS (2004) Philos Trans R Soc Lond A 362:2311
33. Rigby SJ, Al-Obaidi AHR, Lee S-K, McStay D, Robertson PKJ (2006) Appl Surf Sci 252:7948
34. Landi BJ, Cress CD, Evans CM, Raffaelle RP (2005) Chem Mater 17:6819
35. Itkis ME, Perea DE, Jung R, Niyogi S, Haddon RC (2005) J Am Chem Soc 127:3439
36. Tsyboulski DA, Rocha JDR, Bachilo SM, Cognet L, Weisman RB (2007) Nano Lett 7:3080
37. Arnold MS, Green AA, Hulvat JF, Stupp SI, Hersam MC (2006) Nat Nanotechnol 1:60
38. Stakheev AY, Kustov LM (1999) Appl Catal A 188:3
39. Lim S, Ciuparu D, Chen Y, Yang Y, Pfefferle L, Haller GL (2005) J Phys Chem B 109:2285
40. Voss M, Borgmann D, Wedler G (2002) J Catal 212:10
41. de Boer M, Koch EPFM, Blaauw RJ, Stobbe ER, Hoffmann ANJM, Boot LA, van Dillen AJ, Geus JW (1993) Solid State Ionics 63–65:736
42. Arnoldy P, De Jonge JCM, Moulijn JA (1985) J Phys Chem 89:4517
43. Kaluza L, Gulkova D, Vit Z, Zdrazil M (2007) Appl Catal A 324:30
44. Rajagopal S, Marini HJ, Marzari JA, Miranda R (1994) J Catal 147:417
45. Wang HY, Ruckenstein E (2002) Carbon 40:1911
46. Alvarez WE, Kitiyanan B, Borgna A, Resasco DE (2001) Carbon 39:547
47. Ding F, Larsson P, Larsson JA, Ahuja R, Duan HM, Rosen A, Bolton K (2008) Nano Lett 8:463
48. Reich S, Li L, Robertson J (2005) Phys Rev B 72:165423